Geophysical Journal International

*Geophys. J. Int.* (2016) **204,** 1443–1461
GJI Seismology

doi: 10.1093/gji/ggv534

# Using time filtering to control the long-time instability in seismic wave simulation

L. Gao, R. Brossier and J. Virieux

*ISTerre, Univ. Grenoble Alpes, France. E-mail: Longfei.Gao@ujf-grenoble.fr*

Accepted 2015 December 11. Received 2015 November 26; in original form 2015 June 24

## SUMMARY

Long-time instabilities have been observed in various scenarios of numerical simulation for seismic wave propagation. They appear as slowly magnifying spurious oscillations in the seismograms at the late stage of the simulation. Their magnifying speed is typically much slower than the magnifying speed observed when the Courant–Friedrichs–Lewy condition is violated. The simulations can therefore continue to proceed for a relatively long period without floating-point overflow. The impact of the long-time instabilities on the simulation accuracy at the early stage can be negligible in some cases. In existing literatures, spatial-filtering techniques that, in principle, average the solution within certain spatial range at the same time level are typically utilized to control the long-time instability. In this paper, we present an alternative time-filtering approach that, in principle, averages the solution at different time levels of the same spatial location to control the long-time instability. Comparing with the spatial filtering, the advantages of this time-filtering approach lie in its flexibility, particularly when boundaries or interfaces are involved, its simplicity and low additional arithmetic operations, at the expense of extra memory cost. When application of the time filtering is localized to regions where long-time instabilities are emitted from, for example, a boundary or an interface layer, the additional cost is negligible when compared with the cost of wave simulation. For linear wave equations, this time-filtering approach can be understood as the introduction of artificial diffusion. Its application has impact on the accuracy of the solution and the restriction of the time step size. We present an indicator-based approach to adjust the filtering parameters both spatially and temporally, in order to provide the best trade-off between accuracy and stability. The indicator is calculated heuristically by monitoring the spurious oscillation as the simulation evolves in time.

**Key words:** Numerical solutions; Instability analysis; Wave propagation.

## 1 INTRODUCTION

Long-time instabilities, appearing as slowly growing high-frequency oscillations in the seismograms at the late stage of the simulation, have been observed in many simulation scenarios of seismic wave propagation problems, particularly when special boundary or interface treatment is involved. For example, long-time instability was observed in Givoli & Cohen (1995) when attempted to apply a Kirchhoff-type non-reflecting boundary condition. The remedy proposed therein is to use the dissipative Lax–Wendroff scheme, which amounts to introducing a Laplacian type filter in space. Another example is the finite-difference wave modelling with the discontinuous-grid discretization. For example, in both Kristek *et al.* (2010), where staggered grid is considered, and Zhang *et al.* (2013), where full grid is considered, long-time instabilities are observed and controlled successfully with spatial-filtering techniques. The Lanczos filter is proposed in Kristek *et al.* (2010) while the Gaussian filter is proposed in Zhang *et al.* (2013). Furthermore, in Gao *et al.* (2015), long-time instability is also encountered when imposing the free-surface boundary condition in elastic medium for non-flat topography with an immersed boundary method. In order to control the long-time instability, an additional Laplacian term was introduced to the first-order velocity–stress formulation of the wave equation to provide artificial diffusion therein.

Since the long-time instability only affects the late stage of the simulation, while impacts very little on the simulation accuracy at the early stage, they may have been neglected in various cases. As a consequence, there is a lack of substantial discussion on this issue in the geophysical exploration community. For the long-time instability associated with the treatment of flat free surface in elastic wave simulation, we refer the readers to Hestholm (2003), where the first-order velocity–stress formulation is considered and the series work of Stacey (1994, 2000, 2003), where the second-order displacement formulation is considered, as well as Ilan & Loewenthal (1976) for relevant information.

© The Authors 2016. Published by Oxford University Press on behalf of The Royal Astronomical Society.



Downloaded from https://academic.oup.com/gji/article/204/3/1443/677722 by guest on 24 April 2024

However, for more general cases, at least to the knowledge of the authors, the mechanism that generates the long-time instability, which can be case-dependent, has yet to be clearly understood. It is generally suspected that the high-frequency noises incurred by the numerical discretization techniques, particularly those concerning treatment of the boundaries or interfaces, are responsible for the appearance of long-time instability. It is reported in Givoli & Cohen (1995) that the long-time instability appears later for smaller time steps, and for solution with lower-frequency content. It is also reported in Gao *et al.* (2015) that smaller temporal or spatial discretization size can alleviate the long-time instability issue, in terms of both the appearance stage and the frequency range. These observations serve as numerical evidences to the belief that this long-time instability is linked with non-standard numerical discretization.

Among the limited literature in the geophysical exploration community on the long-time instability issue, the spatial averaging or filtering approach is generally utilized to maintain stable simulation. However, in a related research field, that is, the field of meteorological study, where the long-time instabilities are more frequently encountered and battled (e.g. Kurihara 1965; Robert 1966; Asselin 1972; Durran 1991; Williams 2009), the dominant approach to mitigate the long-time instability has been the time filtering. Specifically, the Robert-Asselin (RA) time filter (e.g. Robert 1966; Asselin 1972) and its variants (e.g. Williams 2009, 2013) seem to have been the method of choice in the meteorological community. Intrinsically, the RA filter amounts to introducing the second-order time derivative of the solution, up to a multiplicative coefficient, as an additional term to the underlying equation, as a mechanism to damp out the highly oscillatory modes. Variants of the RA filter that introduce to the equations additional terms that are higher than second-order time derivatives also exist, for example, Marsaleix *et al.* (2012), Williams (2013), Li & Trenchea (2014) and Moustaoui *et al.* (2014).

In this paper, we propose the time-filtering approach, as an alternative to the spatial averaging or filtering approach, to the geophysical exploration community with the aim of controlling the long-time instability. The rest of this paper is organized as follows. We first present several model problems to demonstrate the long-time instability issue. The time-filtering approach is then presented as a remedy to the long-time instability issue. Its mathematical formulation and numerical implementation pertinent to the seismic wave propagation problems will be discussed thoroughly. An indicator-based approach to monitor the long-time instability and adjust the time-filtering parameter dynamically is presented subsequently. Numerical examples are provided in each section to assist the discussion. Finally, we give our perspectives on future research directions and then conclude the paper.

## 2 MODEL PROBLEMS

### 2.1 The Lorenz system

The Lorenz system (Lorenz 1963) is a system of ordinary differential equations (ODEs), simplified from the mathematical model of atmospheric convection. As shown in eq. (1), scalars $x$, $y$ and $z$ are the state variables, depending on the time variable $t$ only. Scalars $\sigma_L$, $\rho_L$ and $\beta_L$ are the deterministic system parameters.

$$\begin{cases} \dfrac{\mathrm{d}x}{\mathrm{d}t} = \sigma_L(y - x); \\ \dfrac{\mathrm{d}y}{\mathrm{d}t} = x(\rho_L - z) - y; \\ \dfrac{\mathrm{d}z}{\mathrm{d}t} = xy - \beta_L z. \end{cases} \tag{1}$$

This simple three-equation nonlinear system is known for its chaotic character and has been widely used as a test platform in the meteorological research field to examine the time filters or time integration schemes in general (e.g. Durran 1991; Li & Trenchea 2014; Moustaoui *et al.* 2014).

To demonstrate the long-time instability issue and its link with the choice of numerical discretization, we solve (1) with the following parameter set: $\sigma_L = 12$, $\rho_L = 12$, $\beta_L = 6$ and initial condition: $x = -10$, $y = -10$, $z = 25$ at time $t = 0$, same as in Durran (1991). We use the MATLAB (MATLAB 2013) command 'ode45' to provide the reference solution, where the time step size is determined automatically and dynamically based on the error estimation by comparing the results of fourth-order Runge–Kutta and fifth-order Runge–Kutta explicit schemes. We also use the leapfrog scheme with two different time step sizes, that is, $\Delta t = 5\text{e-}03\text{s}$ and $\Delta t = 5\text{e-}05\text{s}$, respectively, to solve (1). For all three cases, the simulation is performed for 0.5 s. The time history of variable $x$ is plotted in Fig. 1.

From Fig. 1, we can see that all three solutions agree very well at the early stage of the simulation. However, after around 0.3 s simulation, spurious high-frequency oscillations become observable in the solution corresponding to the leapfrog scheme with a coarse time step size (5e-03 s). On the other hand, simulations using 'ode45' and leapfrog with a fine time step size (5e-05 s) remain stable for 0.5 s.

### 2.2 Non-reflecting boundary condition

In this model problem, we replicate fig. 6 in Givoli & Cohen (1995) to demonstrate the long-time instability caused by the application of a Kirchhoff-type non-reflecting boundary condition (NRBC), originally proposed in Ting & Miksis (1986). The non-dimensionalized 1-D

Downloaded from https://academic.oup.com/gji/article/204/3/1443/677722 by guest on 24 April 2024

wave equation as shown in eq. (2) is considered, where $x \in [0, +\infty)$ and $t \in [0, +\infty)$. The solution is assumed to be at rest for $t < 0$.

$$\begin{aligned} \frac{\partial^2 u}{\partial t^2} &= c^2 \frac{\partial^2 u}{\partial x^2}; \\ u(0, t) &= g(t); \\ u(x, 0) &= \frac{\partial u}{\partial t}(x, 0) = 0. \end{aligned} \tag{2}$$

The exact solution of eq. (2) is

$$u = \begin{cases} g\left(t - \dfrac{x}{c}\right) & \text{if} \quad t \geq \dfrac{x}{c}, \\ 0 & \text{otherwise.} \end{cases} \tag{3}$$

For this simple 1-D model problem, the continuous Kirchhoff-type NRBC takes the form of

$$u(\mathcal{B}_{\text{out}}, t) = u\left(\mathcal{B}_{\text{in}}, t - \frac{(\mathcal{B}_{\text{out}} - \mathcal{B}_{\text{in}})}{c}\right), \tag{4}$$

where $\mathcal{B}_{\text{in}}$ and $\mathcal{B}_{\text{out}}$ are the locations of the prescribed inner and outer boundaries to truncate the semi-infinite medium. Solution in the entire domain $[0, \mathcal{B}_{\text{out}}]$ is of interest. Domain $[\mathcal{B}_{\text{in}}, \mathcal{B}_{\text{out}}]$ is the boundary layer used to absorb the outgoing waves.

The configuration parameters are set as $c = 1$, $g = \sin(t)$, $\mathcal{B}_{\text{out}} = 1$. The simulation domain $[0, \mathcal{B}_{\text{out}}]$ is discretized with 10 grid points, corresponding to grid spacing $\Delta x = 0.1$ while the time step size $\Delta t$ is set as 0.05. We note here that due to the choice that $\mathcal{B}_{\text{in}}$ and $\mathcal{B}_{\text{out}}$ are placed on the grid points, the application of the Kirchhoff-type NRBC (4) is simply an assignment operation. We test the Kirchhoff-type NRBC for two cases, where $\mathcal{B}_{\text{in}} = 0.7$ and $\mathcal{B}_{\text{in}} = 0.9$, respectively.

We discretize eq. (2) with the finite-difference scheme as shown in eq. (5)

$$U_i^{n+1} = 2U_i^n - U_i^{n-1} + \left(\frac{c\Delta t}{\Delta x}\right)^2 \left(U_{i+1}^n - 2U_i^n + U_{i-1}^n\right) \tag{5}$$

for $i \geq 1$ and $n \geq 1$, where $U_i^n$ stands for the discretized solution of $u$ at grid point $i$ and time step $n$. The discretized solution at $i = 0$ and at $n = 0$ are imposed through the boundary condition and initial condition in eq. (2), respectively.

In Fig. 2, we plot the time history of the numerical solution at $\mathcal{B}_{\text{out}}$ for the two test cases, where $\mathcal{B}_{\text{in}} = 0.7$ and $\mathcal{B}_{\text{in}} = 0.9$, respectively, compared against the analytical solution (3). The legend label '$N_{\text{dis}}$' stands for the distance in between $\mathcal{B}_{\text{in}}$ and $\mathcal{B}_{\text{out}}$ in terms of the spatial grid spacing. We kept this label to be consistent with fig. 6 in Givoli & Cohen (1995). $N_{\text{dis}} = 3$ corresponds to $\mathcal{B}_{\text{in}} = 0.7$ while $N_{\text{dis}} = 1$ corresponds to $\mathcal{B}_{\text{in}} = 0.9$. We observe in Fig. 2 that for the case $\mathcal{B}_{\text{in}} = 0.7$, that is, $N_{\text{dis}} = 3$, long-time instability becomes visible after around 15 s simulation while for the case $\mathcal{B}_{\text{in}} = 0.9$, that is, $N_{\text{dis}} = 1$, the simulation maintains stable for 25 s.

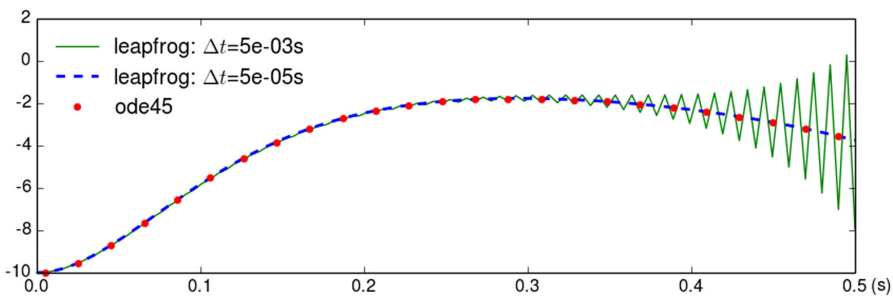


**Figure 1.** Long-time instability is observable for the leapfrog scheme with coarse time step size, that is, $\Delta t = 5\text{e-}03$s.

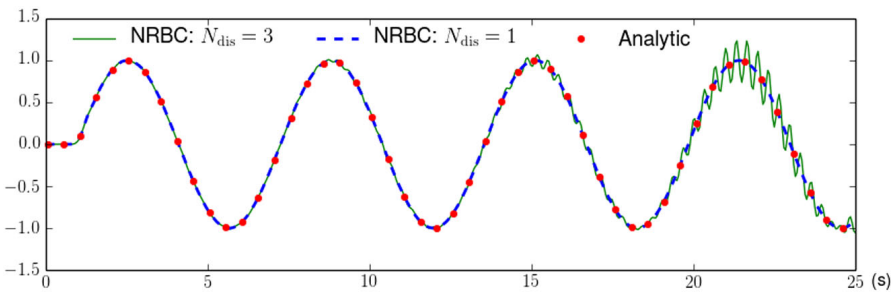


**Figure 2.** Long-time instability becomes visible for the case $\mathcal{B}_{\text{in}} = 0.7$, that is, $N_{\text{dis}} = 3$, after around 15 s simulation.

Downloaded from https://academic.oup.com/gji/article/204/3/1443/677722 by guest on 24 April 2024

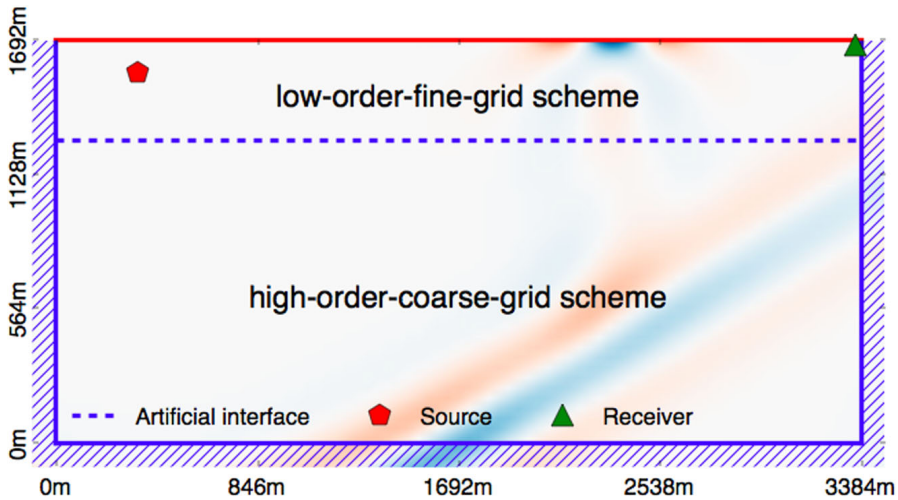


**Figure 3.** Simulation configuration for the model problem of discontinuous-grid simulation.

### 2.3 Discontinuous grid

For real earth model, the near-surface region is usually associated with low velocity speeds, highly heterogeneous media and complex topographic features. Therefore, low-order scheme with fine grid-spacing is preferable for simulation in the near-surface region, due to the accuracy concern. However, using such scheme for the entire simulation domain can be impractical for realistic problems due to the associated heavy computational burden. It is then desirable to separate the numerical discretization of the near-surface region from the rest of the targeted domain, where high-order scheme with coarse grid-spacing is preferable. This leads to the idea of discontinuous-grid simulation, which has been previously investigated in, for instance, Jastram & Behle (1992), Jastram & Tessmer (1994), De Lilla (1997), Robertsson & Holliger (1997), Aoi & Fujiwara (1999), Hayashi *et al.* (2001), Kristek *et al.* (2010) and Zhang *et al.* (2013).

However, long-time instability can arise in discontinuous-grid simulation (e.g. Hayashi *et al.* 2001; Kristek *et al.* 2010; Zhang *et al.* 2013), particularly when the ratio between the coarse and fine grid-spacing is large. The usage of injection as the fine-to-coarse grid transfer operator is believed to be responsible for the appearance of the long-time instability. A spatial averaging approach was proposed in Hayashi *et al.* (2001) to mitigate the long-time instability while a spatial filtering approach was adopted in Kristek *et al.* (2010) and Zhang *et al.* (2013).

In the following, we demonstrate the long-time instability issue associated with the discontinuous-grid simulation by a numerical example. Specifically, we solve the 2-D isotropic elastic wave eq. (6) with the following physical parameters: density $\rho = 1000\,\mathrm{kg\,m^{-3}}$, $P$-wave velocity $\mathcal{V}_P = 5640\,\mathrm{m\,s^{-1}}$ and $S$-wave velocity $\mathcal{V}_S = 2870\,\mathrm{m\,s^{-1}}$. In (6), $V_x$ and $V_z$ stand for the horizontal and vertical particle velocity, respectively; $\sigma_{xx}$, $\sigma_{xz}$ and $\sigma_{zz}$ are the stress components; $\lambda$ and $\mu$ are the elastic Lamé parameters; $S_{\mathcal{R}}$ is the Ricker source term with peak frequency 5 Hz and delay time 0.25 s, applied on the $\sigma_{xx}$ and $\sigma_{zz}$ stress components to mimic an explosion.

$$\begin{cases} \dfrac{\partial V_x}{\partial t} = \dfrac{1}{\rho}\dfrac{\partial \sigma_{xx}}{\partial x} + \dfrac{1}{\rho}\dfrac{\partial \sigma_{xz}}{\partial z}; \\ \dfrac{\partial V_z}{\partial t} = \dfrac{1}{\rho}\dfrac{\partial \sigma_{xz}}{\partial x} + \dfrac{1}{\rho}\dfrac{\partial \sigma_{zz}}{\partial z}; \\ \dfrac{\partial \sigma_{xx}}{\partial t} = (\lambda + 2\mu)\dfrac{\partial V_x}{\partial x} + \lambda\dfrac{\partial V_z}{\partial z} + S_{\mathcal{R}}; \\ \dfrac{\partial \sigma_{xz}}{\partial t} = \mu\dfrac{\partial V_z}{\partial x} + \mu\dfrac{\partial V_x}{\partial z}; \\ \dfrac{\partial \sigma_{zz}}{\partial t} = \lambda\dfrac{\partial V_x}{\partial x} + (\lambda + 2\mu)\dfrac{\partial V_z}{\partial z} + S_{\mathcal{R}}. \end{cases} \tag{6}$$

Fig. 3 illustrates the simulation domain, which is a rectangle with the coordinate on the $x$-direction spans from 0 to 3384 m and the coordinate on the $z$-direction spans from 0 to 1692 m. The $z$-direction is pointed upwards. A horizontal artificial interface is placed at $z = 1269$ m to separate the low-order-fine-grid and high-order-coarse-grid simulation regions. Above the artificial interface, the second-order staggered-grid (Virieux 1986) finite-difference stencil is employed with grid spacing $h = 14.1$ m. Below the artificial interface, the fourth-order staggered-grid stencil (Levander 1988) is employed with grid spacing $H = 42.3$ m. The ratio between the coarse and fine grid-spacing, that is, $H/h$, is 3. In terms of the number of grid points, the fine grid is of size $240 \times 30$ while the coarse grid is of size $80 \times 30$. The leapfrog time integration scheme with time step size $\Delta t = 0.001$ s is used for both regions. Additionally, free-surface boundary condition is imposed at the top border of the rectangular domain while PML layers are appended on the other three borders to mimic a semi-infinite medium. The source is placed at point ($x = 338.4$ m, $y = 1551.0$ m), that is, 141.0 m below the free surface. We record the solution at receiver location ($x = 3355.8$ m, $y = 1670.85$ m), that is, 3017.4 m to the right of the source and 21.15 m below the free surface.

Downloaded from https://academic.oup.com/gji/article/204/3/1443/677722 by guest on 24 April 2024

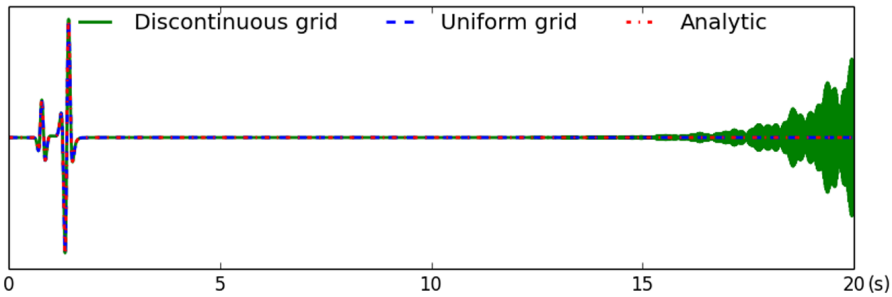


**Figure 4.** The discontinuous-grid simulation exhibits long-time instability at the late stage of the simulation while the uniform-grid simulation remains stable after 20 s simulation.

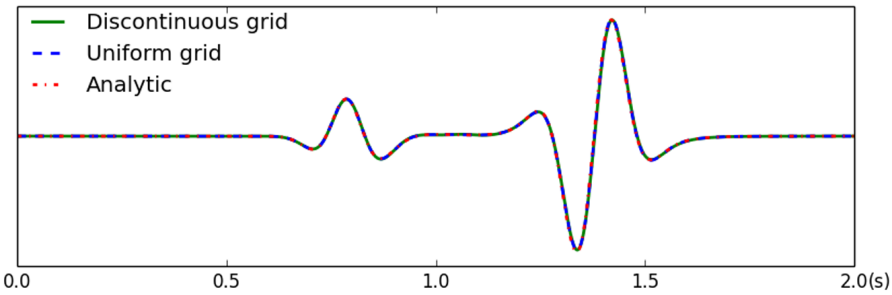


**Figure 5.** The discontinuous-grid simulation result can accurately capture both the body wave and the surface wave at the early stage of the simulation.

The presentation in Kristek *et al.* (2010) has explained very well the mechanism, particularly the grid manipulation, of the discontinuous-grid simulation with the staggered-grid discretization. Although the numerical configuration is slightly different here due to the usage of different spatial-discretization orders in the coarse-grid and fine-grid regions, the concepts therein apply here straightforwardly. Thereby, we refer the readers to Kristek *et al.* (2010) for implementation details regarding the discontinuous-grid simulation with staggered-grid discretization and only highlight our particular choices on several key components in the following.

Specifically, the interface is placed on the subgrid of the normal stress components. The overlap region between the coarse grid and fine grid has thickness of two coarse grids, starting at the interface and extending upwards, towards the free surface. The fine-to-coarse grid transfer is done via injection. This is made possible by deliberately choosing the grid-spacing ratio $H/h$ to be an odd number (3 in this case) so that the coarse grid points is a subset of the fine grid points inside the overlap region. The coarse-to-fine grid transfer is done via linear interpolation. These particular choices of the fine-to-coarse and coarse-to-fine grid transfer operators may not be optimal. However, they suffice to demonstrate the long-time instability issue and the effect of time filtering later on.

With the setup described above, we perform the simulation for 20 000 time steps, that is, 20 s. The simulated seismogram of $V_z$ recorded at the receiver is shown in Fig. 4, compared against the uniform-grid solution and the analytical solution. The uniform-grid solution is simulated using the second-order staggered-grid finite-difference stencil everywhere with grid spacing 14.1 m and leapfrog integration scheme with step size 0.001 s. The analytical solution is calculated with the code provided at http://www.spice-rtn.org/library/software/EX2DVAEL.html for the Garvin's problem (e.g. De Hoop 1960; Berg *et al.* 1994). Figs 5 and 6 display the zoomed-in plots of the first 2 s and the last 2 s of the seismogram shown in Fig. 4, respectively.

From Figs 4–6, we can see that at the early stage of the simulation, the discontinuous-grid solution is accurate for both the body wave (first arrival) and the surface wave (second arrival). However, long-time instability starts to develop at the late stage of the simulation, appearing as the highly oscillatory wave signal in the seismogram, and becomes visible after about 15 s of simulation.

**Remark 1.** In this specific example, the time when the high-frequency oscillation starts to become visible is heavily affected by the simulation configuration. For instance, if we place the interface and the source at 141 and 70.5 m below the free surface, respectively, and

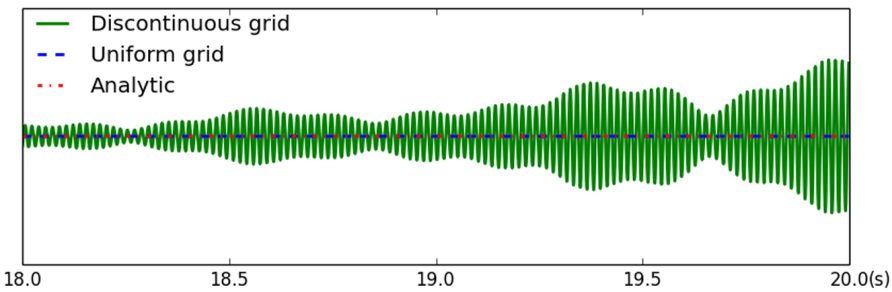


**Figure 6.** Long-time instability occurs at the late stage of the discontinuous-grid simulation, appearing as the highly oscillatory wave signal in the seismogram.

Downloaded from https://academic.oup.com/gji/article/204/3/1443/677722 by guest on 24 April 2024

keep every other parameter unchanged, the amplitude of the high-frequency oscillation will exceed the surface wave amplitude within 8s, much sooner than the example shown in Figs 4–6. On the other hand, the time step size seems to have very little influence on the arrival time of the long-time instability for this example. For instance, the moment when the amplitude of the high-frequency oscillation reaches 5 per cent of the maximum surface wave amplitude is merely postponed to 17.371 s for time step size 0.0005 s, from 17.111 s for time step size 0.001 s.

## 3 TIME FILTERING – A GENERIC APPROACH TO COUNTERBALANCE THE LONG-TIME INSTABILITY

### 3.1 Mathematical description

Given the repeated and widely scattered appearances of the long-time instability, it is desirable to counterbalance it with a generic approach, which does not require significant modification of the underlying numerical methods and meanwhile, can be applied to a wide range of problems. We present the time filtering as one such approach.

By time filtering, we mean replacing the solution at a given time step by a combination of the solution at neighbouring time steps. Given the popularity of the explicit time integration schemes in the seismic community, we will only focus on the kind of time filtering that preserves the explicit character. This means that the solution at the neighbouring time steps used for time filtering are already available when time filtering is applied.

As long as a given time-dependent partial differential equation (PDE) (system) is solved numerically with time integration schemes, we have access to the time history of the entire discretized representation of the solution, readily to be used for time filtering. Therefore, the time-filtering approach is generic to problems described by time-dependent PDEs. Meanwhile, the time filtering acts as a post-processing operation for the time integration scheme at each time step. Its application does not require modification of the underlying discretization methods, but merely requires limited amount of extra calculations and storage space. Therefore, the time-filtering approach is easy to implement and resource-friendly. Moreover, unlike spatial filtering, the time filtering is localized to each spatial grid point. This can be advantageous when the filtering region is close to or include a boundary or interface, in which case the time filtering can be applied readily while the spatial filtering may require extra care for the boundary or interface.

The essence of the time filtering can be illustrated by considering the simple scalar ODE (7), which admits oscillatory solution $u = \mathrm{e}^{\imath\omega t}$ where $\imath = \sqrt{-1}$. Analysis regarding the behaviour of different numerical methods in (7) can be found in Kurihara (1965), Asselin (1972), Durran (1991), Williams (2013) and Li & Trenchea (2014), among others.

$$\frac{\partial u}{\partial t} = \imath\omega u \tag{7}$$

Discretizing eq. (7) with the standard three-level leapfrog scheme leads to the following relation:

$$U^{n+1} - 2\imath\omega\Delta t U^n - U^{n-1} = 0, \tag{8}$$

where $U^n$ is the discretized solution at time step $n$ and $\Delta t$ is the time step size.

Assuming the relation $U^{n+1} = AU^n$ between two neighbouring time steps, we have the following quadratic equation for the amplification rate $A$:

$$A^2 - 2\imath\omega\Delta t A - 1 = 0. \tag{9}$$

Denoting the two solutions of eq. (9) as $A^+$ and $A^-$, respectively, we have

$$\begin{aligned} A^+ &= \imath\omega\Delta t + \sqrt{1-\omega^2\Delta t^2}, \\ A^- &= \imath\omega\Delta t - \sqrt{1-\omega^2\Delta t^2}. \end{aligned} \tag{10}$$

Given $1 - \omega^2\Delta t^2 \geq 0$, both $A^+$ and $A^-$ have modulus 1, which means that the leapfrog scheme is amplitude-preserving. Among the two solutions, $A^+$ corresponds to the physical mode of the solution while $A^-$ corresponds to the computational mode, which is caused by numerical artefacts. For an in-depth analysis about the physical mode and computational mode admitted by the leapfrog scheme, we refer the readers to the course notes at http://kiwi.atmos.colostate.edu/group/dave/at604.html, chapter 4.

Now, let us look at the mechanism and effect of the RA (e.g. Robert 1966; Asselin 1972) time-filtered leapfrog scheme in eq. (7). After obtaining $U^{n+1}$, we filter $U^n$ with the following formula:

$$\overline{U^n} = U^n + \frac{\nu}{2}\left(\overline{U^{n-1}} - 2U^n + U^{n+1}\right), \tag{11}$$

where $\nu > 0$ is the numerical parameter controlling the effectiveness of filtering, $\overline{U^n}$ denotes the filtered solution at time step $n$ and $U^{n+1}$ is the 'raw' solution at time step $n+1$ updated from the following modified leapfrog scheme:

$$\frac{U^{n+1} - \overline{U^{n-1}}}{2\Delta t} = \imath\omega U^n. \tag{12}$$

Downloaded from https://academic.oup.com/gji/article/204/3/1443/677722 by guest on 24 April 2024

Together, eqs (12) and (11) constitute the formulae of the RA-filtered leapfrog scheme. Cancelling out $\overline{U^{n-1}}$ from eqs (11) and (12), we obtain

$$\overline{U^n} = \nu U^{n+1} + [1 - \nu(\imath\omega\Delta t + 1)]U^n.$$

Therefore, we have

$$\overline{U^{n-1}} = \nu U^n + [1 - \nu(\imath\omega\Delta t + 1)]U^{n-1}. \tag{13}$$

Substituting eq. (13) into eq. (12), we obtain the relationship between $U^{n+1}$, $U^n$ and $U^{n-1}$ as in eq. (14):

$$U^{n+1} - (\nu + 2\imath\omega\Delta t)U^n - [1 - \nu(\imath\omega\Delta t + 1)]U^{n-1} = 0. \tag{14}$$

Assuming again that $U^{n+1} = AU^n$, we obtain the quadratic equation for the amplification rate $A$ of the time-filtered leapfrog scheme:

$$A^2 - (\nu + 2\imath\omega\Delta t)A - [1 - \nu(\imath\omega\Delta t + 1)] = 0. \tag{15}$$

The two solutions of eq. (15) are

$$A^+ = \frac{\nu}{2} + \imath\omega\Delta t + \sqrt{\left(1 - \frac{\nu}{2}\right)^2 - \omega^2\Delta t^2}$$

and

$$A^- = \frac{\nu}{2} + \imath\omega\Delta t - \sqrt{\left(1 - \frac{\nu}{2}\right)^2 - \omega^2\Delta t^2}.$$

Once again, $A^+$ corresponds to the physical mode of the solution while $A^-$ corresponds to the computational mode. Given $(1 - \frac{\nu}{2})^2 - \omega^2\Delta t^2 \geq 0$, both $A^+$ and $A^-$ have modulus smaller than 1. Therefore, the simulation will remain stable and the amplitude of the solution will decay as the time step matches forward. Moreover, for the modulus of $A^+$, we have

$$\left|A^+\right|^2 = 1 - \nu\left(1 - \frac{\nu}{2}\right) + \nu\sqrt{\left(1 - \frac{\nu}{2}\right)^2 - \omega^2\Delta t^2}. \tag{16}$$

From (16), we can see that given the same time step size $\Delta t$ and fixed parameter $\nu$, the higher frequency content in the physical solution is damped more severely. We also note that the relation $(1 - \frac{\nu}{2})^2 - \omega^2\Delta t^2 \geq 0$ imposes stronger restriction on the time step size $\Delta t$ than in the case of the unfiltered leapfrog, that is, $1 - \omega^2\Delta t^2 \geq 0$.

We note here that, up to a multiplicative coefficient, the term $\frac{\nu}{2}(\overline{U^{n-1}} - 2U^n + U^{n+1})$ in eq. (11) is an approximation of the second-order time derivative of $u$, that is, $\frac{\partial^2 u}{\partial t^2}$. Therefore, applying time filtering (11) can be linked with modifying the original differential equation by appending a second-order time derivative of the solution. In the case of first-order system of acoustic or elastic wave equations, this is equivalent to introducing a Laplacian type spatial operator to the original wave equations. Intuitively speaking, the diffusive nature of this operator smooths out the solution and in doing so, provides stability for the simulation. As a side-effect, the modelling accuracy can be degraded due to the smoothing. On the other hand, the second-order spatial derivatives in the Laplacian type operator also leads to stronger restriction on the time step size. These connections and effects will be further discussed in the subsequent sections and appendices.

### 3.2 Implementation of the time filtering

In the following, we demonstrate the implementation of the time filtering for the model problems presented in Section Model problems. Since the time-filtering technique is designed based on a modification of the time integration scheme and the temporal differential operators involved in different wave propagation models are simple and similar, we believe that the implementation of the time filtering can be easily transported to other cases.

#### *3.2.1 Lorenz system*

Formulae (11) and (12) can be applied directly to the Lorenz system (1). Using the same configuration as used for Fig. 1 and parameter $\nu = 0.08$, the simulation result for coarse time step size $\Delta t = 5\text{e-}03$s is also stable, as shown in Fig. 7.

#### *3.2.2 NRBC*

For the second-order wave equation presented in eq. (2), instead of eq. (5), we apply the modified leapfrog scheme as shown in eq. (17), which can be linked with modifying the original eq. (2) by appending the fourth-order time derivative of the solution, up to a multiplicative coefficient. Since our main interest here is on the staggered-grid scheme applied on the first-order velocity–stress formulation of the wave equation due to its popularity in the seismic community, we will omit the analysis for scheme (17) on the second-order eq. (2) in the main

Downloaded from https://academic.oup.com/gji/article/204/3/1443/677722 by guest on 24 April 2024

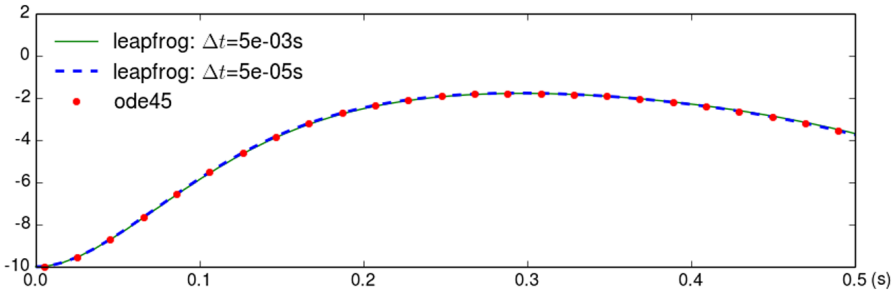


**Figure 7.** Within 0.5 s simulation, long-time instability is no longer observable for the time-filtered leapfrog scheme with coarse time step size, that is, $\Delta t =$ 5e-03s.

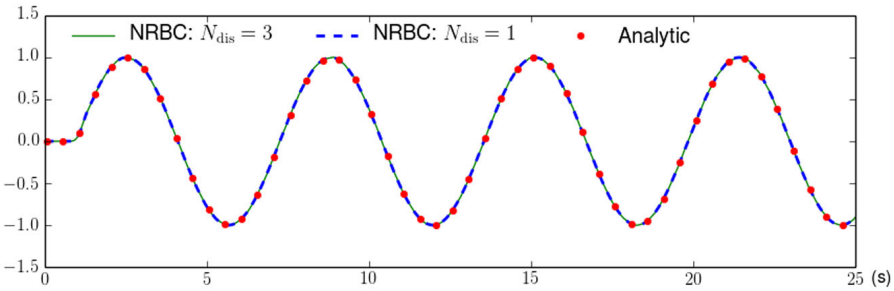


**Figure 8.** Long-time instability is no longer visible for the case $\mathcal{B}_{\rm in} = 0.7$, that is, $N_{\rm dis} = 3$, after 25 s simulation.

body of this paper. For readers who have interest, we refer to Appendix A for more details:

$$T_i^{n-1} = U_{i+1}^{n-1} - 2U_i^{n-1} + U_{i-1}^{n-1}, \tag{17a}$$

$$T_i^{n} = U_{i+1}^{n} - 2U_i^{n} + U_{i-1}^{n}, \tag{17b}$$

$$U_i^{n+1} = 2U_i^{n} - \overline{U_i^{n-1}} + \left(\frac{c\Delta t}{\Delta x}\right)^2 T_i^{n}, \tag{17c}$$

$$T_i^{n+1} = U_{i+1}^{n+1} - 2U_i^{n+1} + U_{i-1}^{n+1}, \tag{17d}$$

$$\overline{U_i^{n}} = U_i^{n} + \beta\left(T_i^{n+1} - 2T_i^{n} + T_i^{n-1}\right). \tag{17e}$$

In eq. (17), eq. (17c) updates the solution according to the wave equation, eq. (17e) filters the solution while eqs (17a), (17b) and (17d) calculate the intermediate variables. In practice, only the quantity $T_i^{n+1}$ is calculated using the formula (17d). Values stored in $T_i^{n-1}$ and $T_i^{n}$ are assigned as the values of $T_i^{n+1}$ from previous time steps. That is why although we have the natural access to the filtered solution $\overline{U_{i-1}^{n-1}}$, $\overline{U_i^{n-1}}$ and $\overline{U_{i+1}^{n-1}}$ when (17a) takes place, the quantity $T_i^{n-1}$ still amounts to being calculated with the unfiltered solution. By doing so, the only extra calculation compared with the unfiltered leapfrog scheme (5) is the application of the time filtering at (17e).

Using the same configuration as used for Fig. 2 and parameter $\beta = -0.02$, the simulation results is stable even for the case with $N_{\rm dis} = 3$, as shown in Fig. 8. The choice of the value of the parameter $\beta$ is also discussed in Appendix A.

### *3.2.3 Discontinuous grid*

Since the application of the time filtering can be localized to each spatial grid point individually and isolated from the way that the spatial derivatives are approximated, we omit the discontinuous-grid spatial-discretization character in the upcoming discussion. Instead, we focus on the application of time filtering on the leapfrog staggered-grid time discretization in general. The resulted algorithm can be applied to the discontinuous grid simulation with no difficulty.

Downloaded from https://academic.oup.com/gji/article/204/3/1443/677722 by guest on 24 April 2024

The idea is to introduce the second-order time derivatives of the wavefield components into the PDE system (6) to provide stabilization, resulting in the following modified PDE system (18).

$$\frac{\partial V_x}{\partial t} = \frac{1}{\rho}\frac{\partial \sigma_{xx}}{\partial x} + \frac{1}{\rho}\frac{\partial \sigma_{xz}}{\partial z} + \beta_x \frac{\partial V_x^2}{\partial t^2}; \tag{18a}$$

$$\frac{\partial V_z}{\partial t} = \frac{1}{\rho}\frac{\partial \sigma_{xz}}{\partial x} + \frac{1}{\rho}\frac{\partial \sigma_{zz}}{\partial z} + \beta_z \frac{\partial V_z^2}{\partial t^2}; \tag{18b}$$

$$\frac{\partial \sigma_{xx}}{\partial t} = (\lambda + 2\mu)\frac{\partial V_x}{\partial x} + \lambda \frac{\partial V_z}{\partial z} + \beta_{xx}\frac{\partial \sigma_{xx}^2}{\partial t^2} + S_{\mathcal{R}}; \tag{18c}$$

$$\frac{\partial \sigma_{xz}}{\partial t} = \mu \frac{\partial V_z}{\partial x} + \mu \frac{\partial V_x}{\partial z} + \beta_{xz}\frac{\partial \sigma_{xz}^2}{\partial t^2}; \tag{18d}$$

$$\frac{\partial \sigma_{zz}}{\partial t} = \lambda \frac{\partial V_x}{\partial x} + (\lambda + 2\mu)\frac{\partial V_z}{\partial z} + \beta_{zz}\frac{\partial \sigma_{zz}^2}{\partial t^2} + S_{\mathcal{R}}. \tag{18e}$$

A rationale behind this modification can be obtained by inspecting the derivation of the Lax–Wendroff scheme, which is known to be dissipative and have the effect of stabilization.

Defining $U$ as the solution vector $[V_x, V_y, \sigma_{xx}, \sigma_{xz}, \sigma_{zz}]^T$, the derivation of the Lax–Wendroff scheme can start by writing out the Taylor expansion of $U^{n+1}$, that is, the evaluation of $U$ at the $n+1$ time step, with respect to time variable $t$:

$$U^{n+1} = U^n + \frac{\Delta t}{1!}\frac{\partial U}{\partial t}\bigg|_n + \frac{\Delta t^2}{2!}\frac{\partial^2 U}{\partial t^2}\bigg|_n + \mathcal{O}(\Delta t^3). \tag{19}$$

The Lax–Wendroff scheme is then derived by substituting the terms $\frac{\partial U}{\partial t}\Big|_n$ and $\frac{\partial^2 U}{\partial t^2}\Big|_n$ in eq. (19) with the homogeneous version of eq. (6), that is, eq. (6) without the source terms, which results in the expression of $U^{n+1}$ in terms of $U$ and its spatial derivatives at time step $n$, hence the two-level Lax–Wendroff scheme. If we reorganize eq. (19) as

$$\frac{U^{n+1} - U^n}{\Delta t} = \frac{\partial U}{\partial t}\bigg|_n + \frac{\Delta t}{2!}\frac{\partial^2 U}{\partial t^2}\bigg|_n + \mathcal{O}(\Delta t^2), \tag{20}$$

it is clear that the application of the Lax–Wendroff scheme to eq. (6) amounts to applying the forward Euler scheme to a modified version of eq. (6) by appending the second-order time derivative of the solution, which provides the dissipative character and stabilization.

In Appendix B, we present the analysis regarding the application of the time-filtered leapfrog staggered-grid scheme on the 1-D wave equation as a further justification. The subsequent question is how to numerically implement this second-order time derivative in the leapfrog staggered-grid time discretization configuration. Although the leapfrog scheme formally involves three different levels of time steps, solution at the middle step is never stored, or even calculated in the staggered time stepping configuration, thanks to the alternating dependence between the velocity and stress components in the velocity–stress formulation (6). This leads to a practical difficulty on time-filtering the leapfrog staggered-grid scheme as we do not have enough time history of the solution to approximate its second-order time derivative.

Denoting the right-hand-sides of the homogeneous version of eq. (6) as $a_x$, $a_z$, $a_{xx}$, $a_{xz}$ and $a_{zz}$, respectively, we observe that $a_x$, $a_z$, $a_{xx}$, $a_{xz}$ and $a_{zz}$ are the first-order time derivatives of $V_x$, $V_z$, $\sigma_{xx}$, $\sigma_{xz}$ and $\sigma_{zz}$, respectively, if the source terms are neglected. At each time step, we obtain the approximations of $a_x$, $a_z$, $a_{xx}$, $a_{xz}$ and $a_{zz}$ through spatial differencing schemes, which can be used to approximate the second-order time derivatives of the solution by central-differencing, provided that we store the approximations of $a_x$, $a_z$, $a_{xx}$, $a_{xz}$ and $a_{zz}$ from the previous time step. This leads to the following time-filtered leapfrog staggered-grid algorithm.

In Algorithm 1, integer $N_T$ stands for the total amount of time steps to be simulated and integer $n$ stands for the current time step. The velocity wavefield components are placed at integer time steps while the stress wavefield components are interlined in the middle of two neighbouring velocity time steps. We use the superscript to indicate the discretized solution at a particular time step.

**Algorithm 1.**

1: **for** $n = 1, N_T$ **do**

2: $\{a_{xx}^n, a_{xz}^n, a_{zz}^n\} \xleftarrow{\text{spatial differencing}} \{V_x^n, V_z^n\}$;

3: $\left\{\sigma_{xx}^{n-1/2}, \sigma_{xz}^{n-1/2}, \sigma_{zz}^{n-1/2}\right\} \xleftarrow{\text{time filtering}} \left\{a_{xx}^n, a_{xz}^n, a_{zz}^n, a_{xx}^{n-1}, a_{xz}^{n-1}, a_{zz}^{n-1}\right\}$;

4: $\left\{\sigma_{xx}^{n+1/2}, \sigma_{xz}^{n+1/2}, \sigma_{zz}^{n+1/2}\right\} \xleftarrow{\text{leapfrog integration}} \left\{a_{xx}^n, a_{xz}^n, a_{zz}^n, \sigma_{xx}^{n-1/2}, \sigma_{xz}^{n-1/2}, \sigma_{zz}^{n-1/2}\right\}$;

5: $\left\{\sigma_{xx}^{n+1/2}, \sigma_{zz}^{n+1/2}\right\} \xleftarrow{\text{source excitation}} \left\{S_{\mathcal{R}}^{n+1/2}\right\}$;

6: $\left\{a_x^{n+1/2}, a_z^{n+1/2}\right\} \xleftarrow{\text{spatial differencing}} \left\{\sigma_{xx}^{n+1/2}, \sigma_{xz}^{n+1/2}, \sigma_{zz}^{n+1/2}\right\}$;

7: $\{V_x^n, V_z^n\} \xleftarrow{\text{time filtering}} \left\{a_x^{n+1/2}, a_z^{n+1/2}, a_x^{n-1/2}, a_z^{n-1/2}\right\}$.

8: $\left\{V_x^{n+1}, V_z^{n+1}\right\} \xleftarrow{\text{leapfrog integration}} \left\{a_x^{n+1/2}, a_z^{n+1/2}, V_x^n, V_z^n\right\}$.

9: **end for**

Downloaded from https://academic.oup.com/gji/article/204/3/1443/677722 by guest on 24 April 2024

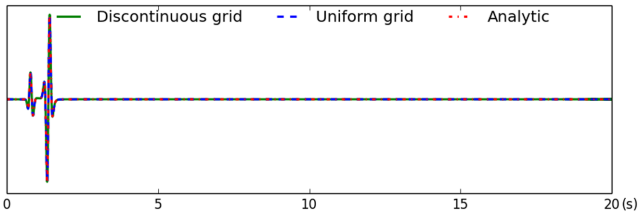


**Figure 9.** The discontinuous-grid simulation is stable with time filtering.

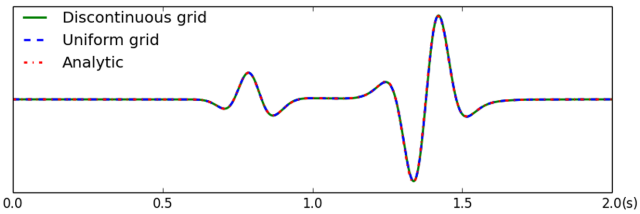


**Figure 10.** The body and surface waves at the early stage of the simulation are still captured accurately.

The spatial differencing schemes used at lines 2 and 6 can be any simple or complicated scheme at choice, and do not have to be uniform for all the spatial grid points. The leapfrog integration scheme at lines 4 and 8 has its usual form as follows:

$$\sigma_{\mathcal{C}}^{n+1/2} = \sigma_{\mathcal{C}}^{n-1/2} + \Delta t a_{\mathcal{C}}^{n},$$

where subscript $_{\mathcal{C}}$ can stand for $_{xx}$, $_{xz}$ or $_{zz}$ and

$$V_{\mathcal{C}}^{n+1} = V_{\mathcal{C}}^{n} + \Delta t a_{\mathcal{C}}^{n+1/2},$$

where subscript $_{\mathcal{C}}$ can stand for $_x$ or $_z$, respectively.

The time filtering at lines 3 and 7 has the form:

$$\overline{\sigma_{\mathcal{C}}^{n-1/2}} = \sigma_{\mathcal{C}}^{n-1/2} + \beta_{\mathcal{C}} \Delta t \left(a_{\mathcal{C}}^{n} - a_{\mathcal{C}}^{n-1}\right), \tag{21}$$

where subscript $_{\mathcal{C}}$ can stand for $_{xx}$, $_{xz}$ or $_{zz}$ and

$$\overline{V_{\mathcal{C}}^{n}} = V_{\mathcal{C}}^{n} + \beta_{\mathcal{C}} \Delta t \left(a_{\mathcal{C}}^{n+1/2} - a_{\mathcal{C}}^{n-1/2}\right), \tag{22}$$

where subscript $_{\mathcal{C}}$ can stand for $_x$ or $_z$, respectively.

We note here that one of the time filtering at line 3 or line 7 in Algorithm 1 can be omitted, yet still provide stabilization to the simulation. We refer the readers to Appendix B for more information. In practice, we may want to omit the time filtering for the wavefield components to which the source excitation is applied, since the source terms are not taken into account in the intuitive derivation presented before.

Recognizing the term $\beta_{\mathcal{C}} \Delta t \left(a_{\mathcal{C}}^{n+1/2} - a_{\mathcal{C}}^{n-1/2}\right)$ in eq. (22) as an approximation of $\beta_{\mathcal{C}} \Delta t^2 \frac{\mathrm{d}^2 V_{\mathcal{C}}^{n}}{\mathrm{d}t^2}$, the coefficient $\beta_{\mathcal{C}} \Delta t^2$ should be at the scale of $\Delta t^2$, motivated by comparing with eq. (19). Similar argument applies to eq. (21). However, the particular choice of $\beta_{\mathcal{C}}$ still needs to be tailored for the underlying problem and algorithm. One may need to go through a trial-and-error process to arrive at the suitable range of parameter choice. For the discontinuous grid simulation presented in the section of Model problems, we choose $\beta_{\mathcal{C}} = 0.02$ for the following simulation test.

Additionally, the time filtering does not have to be applied at all the grid points. Instead, we can localize the application of time filtering to the region where we believe the instability is emitted from. For the case of the discontinuous grid simulation, we only apply the time filtering to the velocity components on the fine grid in the thin horizontal layer where fine-to-coarse grid transfer (injection) takes place, consisting of only six fine-grid points in depth. For a rationale behind this choice of time-filtering region, one can consult the discussion about the mechanism of the long-time instability and its numerical treatment presented in Hayashi *et al.* (2001), Kristek *et al.* (2010) and Zhang *et al.* (2013).

Using the same configuration as being used for Figs 4–6 and parameters $\beta_x = \beta_z = 0.02$ and $\beta_{xx} = \beta_{xz} = \beta_{zz} = 0$, the time-filtered discontinuous grid simulation is stable for 20 s simulation, as shown in Figs 9–11. Moreover, the filtering operation takes roughly 0.95 per cent of the overall computational time for this example.

## 4 ADAPTATION OF THE TIME-FILTERING PARAMETER

### 4.1 Motivation

As demonstrated in the section of Mathematical description, application of the time filtering can effectively damp out the high-frequency noise and ensure stability of the simulation. However, it also decreases the amplitude of the solution as a side effect. Given the propagating nature

Downloaded from https://academic.oup.com/gji/article/204/3/1443/677722 by guest on 24 April 2024

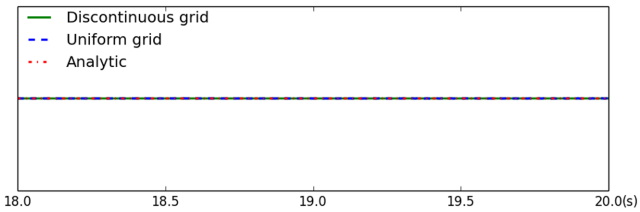


**Figure 11.** Long-time instability does not appear at the late stage of the discontinuous-grid simulation.

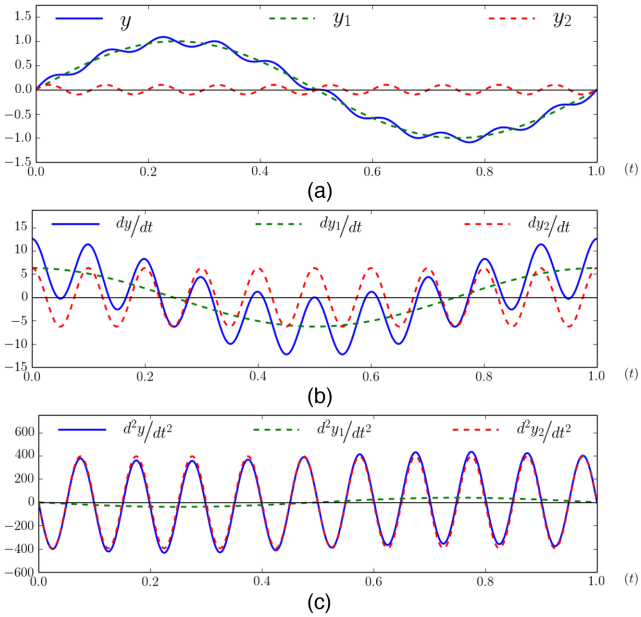


**Figure 12.** Differentiating operation amplifies the presence of the high-frequency component in the composite signal. (a) The composite signal has formula $y = y_1 + y_2$ with $y_1 = \sin(2\pi t)$ and $y_2 = 0.1 \times \sin(20\pi t)$. (b) First-order derivative of the composite signal has formula $\frac{dy}{dt} = \frac{dy_1}{dt} + \frac{dy_2}{dt}$ with $\frac{dy_1}{dt} = 2\pi \sin(2\pi t)$ and $\frac{dy_2}{dt} = 0.1 \times 20\pi \sin(20\pi t)$. (c) Second-order derivative of the composite signal has formula $\frac{d^2y}{dt^2} = \frac{d^2y_1}{dt^2} + \frac{dy_2^2}{dt^2}$ with $\frac{dy_1^2}{dt^2} = (2\pi)^2 \sin(2\pi t)$ and $\frac{dy_2^2}{dt^2} = 0.1 \times (20\pi)^2 \sin(20\pi t)$.

of waves, it is desirable to adapt the time-filtering parameter so that stronger time filtering is applied when and where the high-frequency noise has a stronger presence, and vice versa. This kind of parameter adaptation requires monitoring the solution history. In this section, we provide a heuristic indicator to monitor the presence of high-frequency noise in the solution, based on which the time-filtering parameter is adjusted accordingly.

In the field of meteorology, due to the nonlinearity of the governing PDE systems under interest, the regions where instability arises cannot be predicted in advance. As a result, there, the time filtering is typically applied at the entire simulation domain. Moreover, monitoring the solution history over the entire simulation domain can be very demanding on computational resources. We believe that these are the reasons that adaptation of the time-filtering parameter is not of great interest within the meteorological community.

On the contrary, for the linear wave equations that we are interested in, the long-time instability is typically associated with non-standard numerical treatment for either boundaries or interfaces. Spatially localizing the time filtering to boundary or interface layers accordingly can save both the calculations and memory storage significantly. The associated computational cost is essentially 1-D lower than the cost of the wavefield simulation, which makes it numerically achievable to locally monitor the solution history and adapt the time-filtering parameter.

### 4.2 A heuristic indicator

Intuitively speaking, for a signal oscillates around zero, higher frequency implies that the sign of the signal alternates more frequently. This is evident by comparing Figs 5 and 6, where the appearance of high-frequency noise leads to rapid sign alternation in the seismogram. Therefore, the number of sign alternations within certain number of previous time steps can serve as an indicator of the presence of high-frequency noise. We emphasize here that this kind of indicator is local to each individual spatial grid point, same as the time filtering itself.

However, if high-frequency noise with small amplitude is superposed on a low-frequency signal, it may not lead to rapid sign alternation in the signal itself, as illustrated in Fig. 12(a), where the composite signal $y$ is the sum of low-frequency component $y_1 = \sin(2\pi t)$ and high-frequency component $y_2 = 0.1 \sin(20\pi t)$. Instead, we observe in Figs 12(b) and (c) that the sign alternation in the derivatives of the composite signal is rapid as the differentiating operation effectively amplifies the high-frequency component. Therefore, it is better to use the number of sign alternations in the derivatives of the signal as the indicator as they provides better detection of the high-frequency noise.

Downloaded from https://academic.oup.com/gji/article/204/3/1443/677722 by guest on 24 April 2024

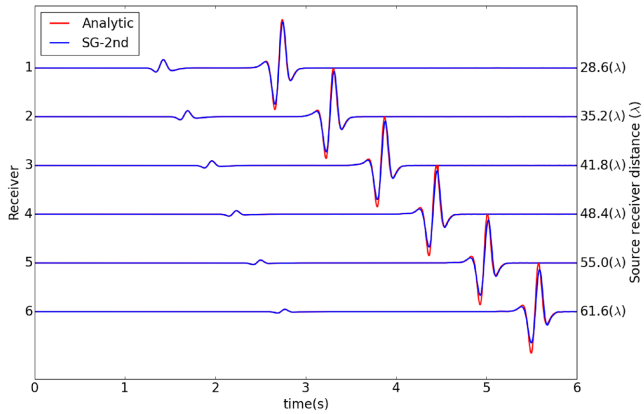


**Figure 13.** Long-time instability is controlled by the introduction of artificial diffusion. Decreased amplitude in the simulated surface wave is obvious.

We note here that in a time-filtered wave simulation algorithm, for example, Algorithm 1, both the first-order and second-order time derivatives of the solution are intermediate results. Specifically, the first-order derivative is approximated for the wavefield updating while the second-order derivative is approximated for the time filtering, *cf.* the term $\frac{(a_f^{n+1/2}-a_f^{n-1/2})}{\Delta t}$ in eq. (22). Higher order derivatives may provide better indication for the long-time instability, but will incur additional cost and complexity. In practice, we always build the indicator based on the second-order time derivative of the solution. The additional calculation incurred by the indicator is merely the counting of the sign alternations while the additional memory needed is merely a register per spatial grid point being filtered. We note here that more complicated indicators may provide better indication and this simple heuristic indicator may not be effective for all cases.

Suppose that we use the number of sign alternations within $N_C$ previous time steps as the indicator, denoted as $S_A$, we present in the following how to link the filtering parameter $\beta_C$ with the indicator $S_A$. For a pure sinusoid with single frequency $f$, the number of sign alternations within $N_C$ time steps is roughly $2\frac{N_C}{\frac{(1/f)}{\Delta t}}$. We select two frequencies $f_{\min}$ and $f_{\max}$, leading to indicator values $N_{C,\min}$ and $N_{C,\max}$ respectively, and associate filtering parameters $\beta_{C,\min}$ and $\beta_{C,\max}$ respectively. $N_{C,\min}$ corresponds to the point where the presence of high-frequency noise starts to be plausible while $N_{C,\max}$ corresponds to the point where the presence of high-frequency noise is more certain. $\beta_{C,\min}$ does not have to be zero, in which case some background time filtering is applied as a prevention measure, regardless of the indicator value. The time-filtering parameter $\beta_C$ is determined using the formula in eq. (23). In other words, $\beta_C$ is determined through linear interpolation when $N_C$ is in between $N_{C,\min}$ and $N_{C,\max}$.

$$\beta_C = \begin{cases} \beta_{C,\min} & \text{if} \quad N_C \le N_{C,\min}; \\ \beta_{C,\min} + \dfrac{(\beta_{C,\max} - \beta_{C,\min})}{(N_{C,\max} - N_{C,\min})}(N_C - N_{C,\min}) & \text{if} \quad N_{C,\min} < N_C < N_{C,\max}; \\ \beta_{C,\max} & \text{if} \quad N_C \ge N_{C,\max}. \end{cases} \tag{23}$$

### 4.3 Numerical example

When the wave travels through the filtering layer transversely, as in the case of the discontinuous-grid simulation with time filtering in the interface layer, the decrease of amplitude in the seismogram is hard to observe as the interaction between the wave and the filtering layer is limited. The decrease of amplitude can be observed more obviously when the wave travels alongside the filtering layer, as in the case of surface wave simulation with time filtering in the free-surface layer. In the following, we demonstrate the benefit of using adaptive time-filtering parameter with an example involving surface wave propagation.

Specifically, we use the same simulation configuration as in example 1 of Gao *et al.* (2015), where long-time instability is observed when applying an immersed free-surface boundary treatment. The accompanying code can be downloaded at http://seiscope2.obs.ujf-grenoble.fr/IMG/zip/IBT_codes.zip. We briefly sketch the simulation configuration in the following and refer the readers to Gao *et al.* (2015) for more details.

The isotropic elastic wave equation in velocity–stress formulation with density $\rho = 1000\,\mathrm{kg\,m^{-3}}$, $P$-wave velocity $\mathcal{V}_P = 5640\,\mathrm{m\,s^{-1}}$ and $S$-wave velocity $\mathcal{V}_S = 2870\,\mathrm{m\,s^{-1}}$ is simulated on a 2-D quadrilateral domain with the free surface tilted for roughly 30° from the horizontal line. Explosive source with Ricker wavelet of 5 Hz peak frequency is applied at 141 m below the free surface, which is within one minimum $S$-wavelength and close enough to generate strong surface wave. Second-order staggered-grid finite-difference stencil and leapfrog integration scheme are used for wavefield simulation. The free-surface boundary condition is imposed through the immersed boundary method described in Gao *et al.* (2015).

In example 1 of Gao *et al.* (2015), the long-time instability is controlled by the introduction of artificial diffusion to the velocity updating equations, which amounts to spatial filtering, obtaining the seismograms of $V_z$ as shown in Fig. 13, which is identical to fig. 3 of Gao *et al.* (2015). On the right-side $y$-label of Fig. 13, λ stands for the minimal $S$-wavelength, which is 229.6 m, corresponding to $S$-wave velocity

Downloaded from https://academic.oup.com/gji/article/204/3/1443/677722 by guest on 24 April 2024

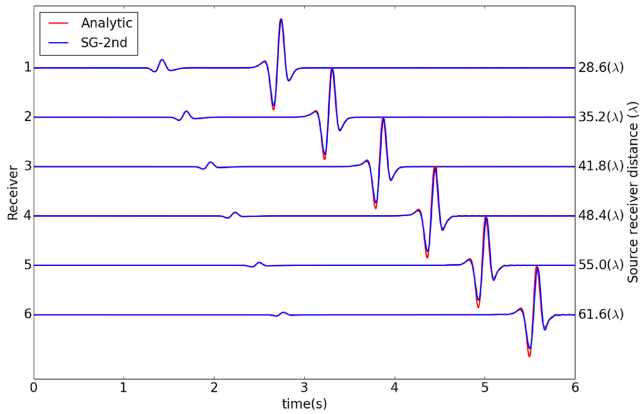


**Figure 14.** Long-time instability is controlled by time filtering with fixed parameter.

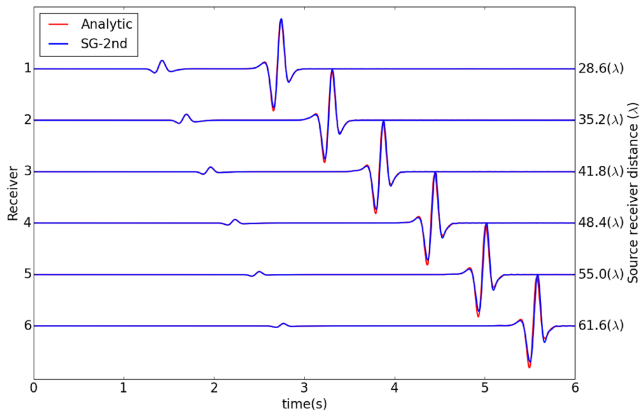


**Figure 15.** Long-time instability is controlled by time filtering with adaptive parameter.

2870 m s$^{-1}$ and maximum frequency 12.5 Hz. The finite-difference solution demonstrates good agreement with the analytic solution, which is generated by the source code provided at http://www.spice-rtn.org/library/software/EX2DVAEL.html for the Garvin's problem. However, decreased amplitude of the surface wave in the finite-difference solution can be observed from the comparison, as a side effect of the artificial diffusion.

Alternatively, we can control the long-time instability through time filtering. Applying time filtering, localized to the thin layer beneath the free surface that consists of 3 grid points, on the velocity components only with fixed filtering parameter $\beta_x = \beta_z = 0.5$, which leads to the most satisfactory result among performed simulation tests with fixed filtering parameter, we obtain the seismograms as shown in Fig. 14, where the amplitude agreement of the surface wave is much better than in Fig. 13.

On the other hand, using adaptive filtering parameter with $\beta_{z,\min} = 0.05$, $\beta_{z,\max} = 1$, $f_{\min} = 5$, $f_{\max} = 10$ and indicator based on monitoring the second-order time-derivative of $V_z$, we obtain the seismograms as shown in Fig. 15. Filtering parameter $\beta_x$ is simply assigned the value of $\beta_z$ at the nearby grid point. The filtering operation takes roughly 0.39 per cent of the overall computational time. We note here that due to the numerical dispersion associated with leapfrog and staggered-grid scheme, if without any filtering, the simulated surface wave would overshoot its analytical counterpart at the crest while undershoot at the trough, *cf.* fig. 4 of Gao *et al.* (2015). We observe that in Fig. 15, the simulated surface wave keeps this character whereas in Fig. 14, the simulated surface wave undershoots its analytical counterpart at both the crest and the trough. Therefore, comparing the results in Figs 14 and 15, we consider the time filtering for Fig. 15, that is, with adaptive filtering parameter, as the one that provides better balance between accuracy and stability.

This subtle visual difference can be better illustrated by the time-frequency misfit quantification (TFMQ; *cf.* Kristeková *et al.* 2006, 2009). We use the same criteria as in Gao *et al.* (2015) for TFMQ, which is repeated in the following for integrity. Specifically, the analytic solution is used as the reference solution while global normalization is applied to obtain the misfit quantification results. The frequency content range is specified as [0.05 Hz, 50 Hz]. Using the terminologies in Kristeková *et al.* (2006, 2009), the single-valued time-domain envelope misfit (term max (abs(TEM)) in the User's guide) and the single-valued time-domain phase misfit (term max (abs(TPM)) in the User's guide) are presented in Tables 1 and 2 as the measurement of the amplitude misfit and phase misfit, correspondingly. The source code used for TFMQ is downloaded from http://www.nuquake.eu/Computer_Codes/index.html. Tables 1 and 2 confirm that using adaptive filtering parameter does have less impact on the surface wave amplitude.

Downloaded from https://academic.oup.com/gji/article/204/3/1443/677722 by guest on 24 April 2024

**Table 1.** Amplitude misfits corresponding to Figs 13–15.

| | Fig. 13 | Fig. 14 | Fig. 15 |
|---|---|---|---|
| Receiver 1 | 9.1E-02 | 5.6E-02 | 3.6E-02 |
| Receiver 2 | 1.1E-01 | 6.7E-02 | 4.2E-02 |
| Receiver 3 | 1.3E-01 | 7.8E-02 | 4.9E-02 |
| Receiver 4 | 1.4E-01 | 9.1E-02 | 5.7E-02 |
| Receiver 5 | 1.6E-01 | 1.0E-01 | 6.3E-02 |
| Receiver 6 | 1.7E-01 | 1.1E-01 | 6.8E-02 |

**Table 2.** Phase misfits corresponding to Figs 13–15.

| | Fig. 13 | Fig. 14 | Fig. 15 |
|---|---|---|---|
| Receiver 1 | 3.4E-02 | 3.3E-02 | 3.4E-02 |
| Receiver 2 | 4.1E-02 | 4.0E-02 | 4.1E-02 |
| Receiver 3 | 4.7E-02 | 4.6E-02 | 4.8E-02 |
| Receiver 4 | 5.5E-02 | 5.3E-02 | 5.6E-02 |
| Receiver 5 | 6.1E-02 | 6.0E-02 | 6.4E-02 |
| Receiver 6 | 6.7E-02 | 6.6E-02 | 7.0E-02 |

## 5 FUTURE PROSPECTS

At this moment, the precise applicable scope of the proposed time-filtering technique is still unclear. Based on the facts that the time-filtering technique is designed based on a modification of the time integration scheme, and the temporal differential operators involved in different wave propagation models are similar and simple, we are optimistic about its portability to other simulation scenarios, such as the viscoelastic or anisotropic media. In particular, we think it may improve the stability of the acoustic anisotropic wave simulation. However, its effectiveness and influence for other simulation scenarios still require extensive study and careful validation on a case-by-case basis, which will be left for future study.

On the other hand, the time-filtering technique that we presented here is an adaptation of the simple RA-filter developed in the meteorological community. More sophisticated time-filtering techniques have been developed for meteorological study. Their applicability and necessity to instabilities arising in the seismic wave simulations remain to be studied.

## 6 CONCLUSIONS

In this paper, we demonstrated the issue of long-time instability in seismic wave simulations, associated with non-standard boundary or interface treatment, by the display of several model problems. The time-filtering technique is presented as a generic approach to remedy the long-time instability, which acts as a post-processing step on the time integration scheme. It has the advantages of being flexible with respect to boundaries or interfaces with low additional cost, particularly when its application is restricted to boundary or interface layers. Mathematical analysis and numerical examples have been presented to demonstrate its effectiveness on controlling long-time instability, as well as its side-effects on accuracy and time step size restriction. Finally, an indicator-based dynamical adjustment of the filtering parameter is presented to provide better balance between accuracy and stability. We believe that the time-filtering technique, which is easy to comprehend and implement, can be useful to the seismic community on providing reliable simulation.

## ACKNOWLEDGEMENTS

This study was partially funded by the SEISCOPE consortium (http://seiscope2.osug.fr), sponsored by BP, CGG, CHEVRON, EXXON-MOBIL, JGI, PETROBRAS, SAUDI ARAMCO, SCHLUMBERGER, SHELL, SINOPEC, STATOIL, TOTAL and WOODSIDE. This study was granted access to the HPC resources of the Froggy platform of the CIMENT infrastructure (https://ciment.ujf-grenoble.fr), which is supported by the Rhône-Alpes region (GRANT CPER07_13 CIRA), the OSUG@ 2020 labex (reference ANR10 LABX56) and the Equip Meso project (reference ANR-10-EQPX-29-01) of the programme Investissements d'Avenir supervised by the Agence Nationale pour la Recherche, and the HPC resources of CINES/IDRIS under the allocation 046091 made by GENCI.

## REFERENCES

Aoi, S. & Fujiwara, H., 1999. 3D finite-difference method using discontinuous grids, *Bull. seism. Soc. Am.,* **89**(4), 918–930.

Asselin, R., 1972. Frequency filter for time integrations, *Mon. Weather Rev.,* **100**(6), 487–490.

Berg, P., If, F., Nielsen, P. & Skovgaard, O., 1994. Analytical reference solutions, in *Modeling the Earth for Oil Exploration,* pp. 421–427, ed. Helbig, K., Pergamon Press.

De Hoop, A., 1960. A modification of Cagniard's method for solving seismic pulse problems, *Appl. Sci. Res. B,* **8**(1), 349–356.

De Lilla, A., 1997. Finite difference seismic wave propagation using variable grid sizes, *Master's thesis,* Massachusetts Institute of Technology.

Durran, D.R., 1991. The third-order Adams-Bashforth method: An attractive alternative to leapfrog time differencing, *Mon. Weather Rev.,* **119**(3), 702–720.

Downloaded from https://academic.oup.com/gji/article/204/3/1443/677722 by guest on 24 April 2024

Gao, L., Brossier, R., Pajot, B., Tago, J. & Virieux, J., 2015. An immersed free-surface boundary treatment for seismic wave simulation, *Geophysics,* **80**(5), T193–T209.
Givoli, D. & Cohen, D., 1995. Nonreflecting boundary conditions based on Kirchhoff-type formulae, *J. Comput. Phys.,* **117**(1), 102–113.
Hayashi, K., Burns, D.R. & Toksöz, M.N., 2001. Discontinuous-grid finite-difference seismic modeling including surface topography, *Bull. seism. Soc. Am.,* **91**(6), 1750–1764.
Hestholm, S., 2003. Elastic wave modeling with free surfaces: stability of long simulations, *Geophysics,* **68**(1), 314–321.
Ilan, A. & Loewenthal, D., 1976. Instability of finite difference schemes due to boundary conditions in elastic media, *Geophys. Prospect.,* **24**(3), 431–453.
Jastram, C. & Behle, A., 1992. Acoustic modelling on a grid of vertically varying spacing, *Geophys. Prospect.,* **40**(2), 157–169.
Jastram, C. & Tessmer, E., 1994. Elastic modelling on a grid with vertically varying spacing, *Geophys. Prospect.,* **42**(4), 357–370.
Kristek, J., Moczo, P. & Galis, M., 2010. Stable discontinuous staggered grid in the finite-difference modelling of seismic motion, *Geophys. J. Int.,* **183**(3), 1401–1407.
Kristeková, M., Kristek, J., Moczo, P. & Day, S.M., 2006. Misfit criteria for quantitative comparison of seismograms, *Bull. seism. Soc. Am.,* **96**(5), 1836–1850.
Kristeková, M., Kristek, J. & Moczo, P., 2009. Time-frequency misfit and goodness-of-fit criteria for quantitative comparison of time signals, *Geophys. J. Int.,* **178**(2), 813–825.
Kurihara, Y., 1965. On the use of implicit and iterative methods for the time integration of the wave equation, *Mon. Weather Rev.,* **93**(1), 33–46.
Levander, A.R., 1988. Fourth-order finite-difference P-SV seismograms, *Geophysics,* **53**(11), 1425–1436.
Li, Y. & Trenchea, C., 2014. A higher-order Robert-Asselin type time filter, *J. Comput. Phys.,* **259,** 23–32.
Lorenz, E.N., 1963. Deterministic nonperiodic flow, *J. Atmos. Sci.,* **20**(2), 130–141.
Marsaleix, P., Auclair, F., Duhaut, T., Estournel, C., Nguyen, C. & Ulses, C., 2012. Alternatives to the Robert-Asselin filter, *Ocean Modelling,* **41,** 53–66.
MATLAB, 2013. MATLAB, version 8.1 (R2013a), The MathWorks Inc., Natick, MA.
Moustaoui, M., Mahalov, A. & Kostelich, E.J., 2014. A numerical method based on leapfrog and a fourth-order implicit time filter, *Mon. Weather Rev.,* **142**(7), 2545–2560.
Robert, A.J., 1966. The integration of a low order spectral form of the primitive meteorological equations, *J. Meteorol. Soc. Japan,* **44,** 237–245.
Robertsson, J. & Holliger, K., 1997. Modeling of seismic wave propagation near the earth's surface, *Phys. Earth planet. Inter.,* **104**(1), 193–211.
Stacey, R., 1994. New finite-difference methods for free surfaces with a stability analysis, *Bull. seism. Soc. Am.,* **84**(1), 171–184.
Stacey, R., 2000. Extending the stability range of the composed approximation for free surfaces, *Bull. seism. Soc. Am.,* **90**(4), 1113–1116.
Stacey, R., 2003. Stability analysis of finite-difference approximations of elastic wave equations, *Bull. seism. Soc. Am.,* **93**(3), 1198–1211.
Ting, L. & Miksis, M.J., 1986. Exact boundary conditions for scattering problems, *J. acoust. Soc. Am.,* **80**(6), 1825–1827.
Virieux, J., 1986. P-SV wave propagation in heterogeneous media: velocity–stress finite-difference method, *Geophysics,* **51**(4), 889–901.
Williams, P.D., 2009. A proposed modification to the Robert-Asselin time filter, *Mon. Weather Rev.,* **137**(8), 2538–2546.
Williams, P.D., 2013. Achieving seventh-order amplitude accuracy in leapfrog integrations, *Mon. Weather Rev.,* **141**(9), 3037–3051.
Zhang, Z., Zhang, W., Li, H. & Chen, X., 2013. Stable discontinuous grid implementation for collocated-grid finite-difference seismic wave modelling, *Geophys. J. Int.,* **192**(3), 1179–1188.

## APPENDIX A: ANALYSIS OF THE TIME-FILTERED LEAPFROG SCHEME ON THE 1-D SECOND-ORDER DISPLACEMENT FORMULATION OF THE WAVE EQUATION

Here, we provide the von Neumann analysis results associated with the second-order wave equation (2) and its numerical scheme (17).

Using $\alpha$ to denote the constant $(\frac{c\Delta t}{\Delta x})^2$, we have relations

$$U_i^{n+1} = 2U_i^n - \overline{U_i^{n-1}} + \alpha\left(U_{i+1}^n - 2U_i^n + U_{i-1}^n\right) \tag{A1}$$

and

$$\overline{U_i^{n-1}} = U_i^{n-1} + \beta\Big(\left(U_{i+1}^n - 2U_i^n + U_{i-1}^n\right) - 2\left(U_{i+1}^{n-1} - 2U_i^{n-1} + U_{i-1}^{n-1}\right) + \left(U_{i+1}^{n-2} - 2U_i^{n-2} + U_{i-1}^{n-2}\right)\Big), \tag{A2}$$

derived from eqs (17c) and (17e), respectively.

Cancelling out $\overline{U_i^{n-1}}$ from eqs (A1) and (A2), we obtain the following relation concerning only the unfiltered solution:

$$\left(U_i^{n+1} - 2U_i^n + U_i^{n-1}\right) + (\beta - \alpha)\left(U_{i+1}^n - 2U_i^n + U_{i-1}^n\right) - 2\beta\left(U_{i+1}^{n-1} - 2U_i^{n-1} + U_{i-1}^{n-1}\right) + \beta\left(U_{i+1}^{n-2} - 2U_i^{n-2} + U_{i-1}^{n-2}\right) = 0. \tag{A3}$$

Considering a single spatial discrete Fourier mode $e^{\imath i\Delta x\xi}$ of the solution and assuming the amplification rate of this mode between two neighbouring steps is $A$, the above relation leads to the cubic eq. (A4) for $A$

$$A^3 + [(\beta - \alpha)\gamma - 2]A^2 + (1 - 2\beta\gamma)A + \beta\gamma = 0, \tag{A4}$$

where $\gamma = e^{\imath\Delta x\xi} - 2 + e^{-\imath\Delta x\xi}$, or $\gamma = 2\cos(\Delta x\xi) - 2$ in terms of trigonometric functions.

Given a fixed $\Delta x$, the highest spatial frequency that can be represented by the grid is $\xi = \frac{\pi}{\Delta x}$, corresponding to the case when the wave signal alternates sign between every two neighbouring spatial grid points. The lowest spatial frequency that can be represented is $\xi = \frac{\pi}{N_x\Delta x}$, where $N_x$ is the number of total spatial discretization points, corresponding to the case where the entire domain only represents half of the wavelength. Therefore, we have $\frac{\pi}{N_x} \le \Delta x\xi \le \pi$. For simplicity and generality, we relax the lower bound to 0, corresponding to an infinite length medium, and obtain $0 < \Delta x\xi \le \pi$. Consequently, we have $0 > \gamma \ge -4$ with $\gamma$ close to 0 corresponding to low-frequency mode and $\gamma$ close to $-4$ corresponding to high-frequency mode.

The analytic formulae for the roots of eq. (A4) is very complicated, we omit the messy expressions here. Instead, we demonstrate the amplitude change of $A$ with respect to parameters $\beta$ and $\gamma$ in Fig. A1. For the parameter ranges that we choose, eq. (A4) exhibits one real root, whose modulus is shown in Fig. A1(a), and two complex conjugate roots, which have the same modulus, shown in Fig. A1(b). Fig. A1(a) corresponds to the computational mode whereas Fig. A1(b) corresponds to the physical modes.

Downloaded from https://academic.oup.com/gji/article/204/3/1443/677722 by guest on 24 April 2024

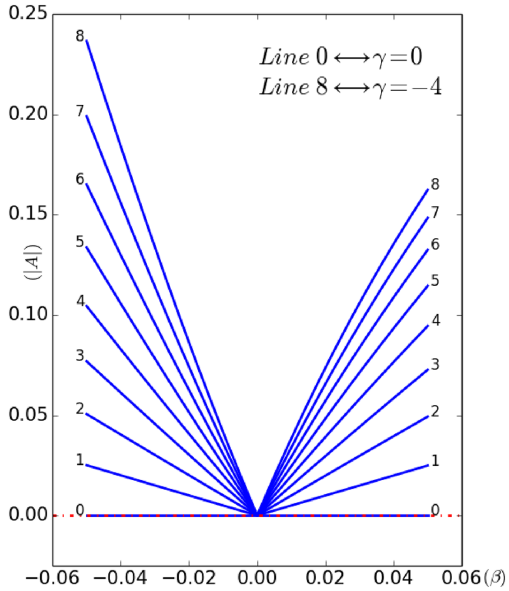


(a)

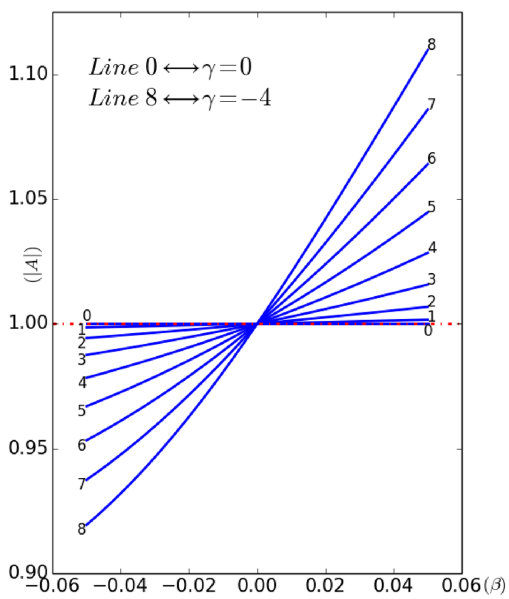


(b)

**Figure A1.** Amplitude change of $A$, as roots of eq. (A4), with respect to parameters $\beta$ and $\gamma$. (a) Amplitude of the real root of $A$ (b) Amplitude of the complex roots of $A$

In Fig. A1, the horizontal axis corresponds to the parameter $\beta$, the vertical axis corresponds to the modulus of $A$ while different lines correspond to different values of $\gamma$. Specifically, lines 0–8 correspond to the anchor points that equidistantly section the interval $[-4, 0]$ with line 0 corresponds to $\gamma = 0$ and line 8 corresponds to $\gamma = -4$. Line 0 coincides with $|A| = 0$ in Fig. A1(a) and $|A| = 1$ in Fig. A1(b), respectively. This is easy to see by setting $\gamma = 0$ in eq. (A4) , which then reduces to $A(A-1)^2 = 0$. The value of $\alpha$ is set to be 0.25, which corresponds to the choice of $\Delta t = 0.05$ and $\Delta x = 0.1$ in the leapfrog scheme (5).

From Fig. A1, it is clear that by setting $\beta$ to a small negative number, all three roots of eq. (A4) have amplitude smaller than 1, which leads to stable simulation. Specifically, we used $\beta = -0.02$ in the simulation for Fig. 8. For the wave equation presented in eq. (2), the input signal has temporal frequency $1/2\pi$. Given that the wave velocity $c = 1$, the spatial frequency is also $1/2\pi$, which corresponds to $\gamma \approx -2.5\text{e-}4$. It then follows that the modulus of the roots corresponding to the physical modes is roughly $1 - 1.6\text{e-}10$. Thereby, for this specific case, the impact of time filtering on the accuracy of the frequency that we are solving for is negligible.

We note here that Fig. A1 does not automatically give us the best choice of $\beta$ since we typically do not know what is the frequency (range) of the numerical noise that causes the long-time instability. The choice of $\beta$ still needs to go through a trial-and-error process. However,

Downloaded from https://academic.oup.com/gji/article/204/3/1443/677722 by guest on 24 April 2024

Fig. A1 do tell us the sign and a rough range of $\beta$ to search for, as well as providing us a quantification of the time-filtering impact on the accuracy of the frequency (range) that we are interested in.

## APPENDIX B: ANALYSIS OF THE TIME-FILTERED LEAPFROG STAGGERED-GRID SCHEME ON THE 1-D FIRST-ORDER VELOCITY–STRESS FORMULATION OF THE WAVE EQUATION

Here, we provide the von Neumann analysis results associated with the application of the time-filtered leapfrog staggered-grid scheme on the first-order formulation of the 1-D wave equation as shown in eq. (B1).

$$\frac{\partial V}{\partial t} = C_V \frac{\partial \sigma}{\partial x}; \tag{B1a}$$

$$\frac{\partial \sigma}{\partial t} = C_\sigma \frac{\partial V}{\partial x}, \tag{B1b}$$

where the parameters $C_V$ and $C_\sigma$ can be chosen as, for instance, $C_V = \frac{1}{\rho}$ and $C_\sigma = \rho c^2$. Since the von Neumann analysis concerns only the interior of the simulation domain, we omit the boundary conditions here. Also omitted is the mechanism that generates the wave, such as the source terms or initial conditions.

First, we consider the leapfrog staggered-grid scheme with time filtering on both $V$ and $\sigma$, as shown in eq. (B2).

$$\text{(filtering)} \qquad \overline{\sigma_{i+1/2}^{n-1/2}} = \sigma_{i+1/2}^{n-1/2} + \beta_\sigma \left[ \left( V_{i+1}^n - V_i^n \right) - \left( V_{i+1}^{n-1} - V_i^{n-1} \right) \right], \tag{B2a}$$

$$\text{(filtering)} \qquad \overline{\sigma_{i-1/2}^{n-1/2}} = \sigma_{i-1/2}^{n-1/2} + \beta_\sigma \left[ \left( V_i^n - V_{i-1}^n \right) - \left( V_i^{n-1} - V_{i-1}^{n-1} \right) \right], \tag{B2b}$$

$$\text{(updating)} \qquad \sigma_{i+1/2}^{n+1/2} = \overline{\sigma_{i+1/2}^{n-1/2}} + \alpha_\sigma (V_{i+1}^n - V_i^n), \tag{B2c}$$

$$\text{(updating)} \qquad \sigma_{i-1/2}^{n+1/2} = \overline{\sigma_{i-1/2}^{n-1/2}} + \alpha_\sigma (V_i^n - V_{i-1}^n), \tag{B2d}$$

$$\text{(filtering)} \qquad \overline{V_i^n} = V_i^n + \beta_V \left[ \left( \sigma_{i+1/2}^{n+1/2} - \sigma_{i-1/2}^{n+1/2} \right) - \left( \sigma_{i+1/2}^{n-1/2} - \sigma_{i-1/2}^{n-1/2} \right) \right], \tag{B2e}$$

$$\text{(updating)} \qquad V_i^{n+1} = \overline{V_i^n} + \alpha_V \left( \sigma_{i+1/2}^{n+1/2} - \sigma_{i-1/2}^{n+1/2} \right), \tag{B2f}$$

where $\alpha_V = C_V \frac{\Delta t}{\Delta x}$ and $\alpha_\sigma = C_\sigma \frac{\Delta t}{\Delta x}$ while $\beta_V$ and $\beta_\sigma$ are the time-filtering parameters. We note here that when the filtering of $\overline{V_i^n}$ takes place at eq. (B2e), the quantities $\sigma_{i+1/2}^{n-1/2}$ and $\sigma_{i-1/2}^{n-1/2}$ are already filtered. However, in practice, instead of repeating the calculation, we would prefer to store the difference $(\sigma_{i+1/2}^{n-1/2} - \sigma_{i-1/2}^{n-1/2})$ from the previous time step when updating $V_i^n$, which is calculated before the filtering of $\sigma_{i+1/2}^{n-1/2}$ and $\sigma_{i-1/2}^{n-1/2}$, and reuse it in the filtering of $\overline{V_i^n}$. This is the reason that the unfiltered $\sigma_{i+1/2}^{n-1/2}$ and $\sigma_{i-1/2}^{n-1/2}$ appear in eq. (B2e), instead of their filtered versions. Same argument applies to eqs (B2a) and (B2b) as well.

Following the same procedure as in Appendix A, we arrive at the cubic eq. (B3) for the amplification rate $A$ between two neighbouring time steps of the chosen Fourier mode,

$$A^3 - (2 + \beta_V \beta_\sigma \gamma + \beta_V \alpha_\sigma \gamma + \alpha_V \beta_\sigma \gamma + \alpha_V \alpha_\sigma \gamma) A^2 + (1 + 2\beta_V \beta_\sigma \gamma + \beta_V \alpha_\sigma \gamma + \alpha_V \beta_\sigma \gamma) A - \beta_V \beta_\sigma \gamma = 0, \tag{B3}$$

where $\gamma = \mathrm{e}^{\imath \Delta x \xi} - 2 + \mathrm{e}^{-\imath \Delta x \xi}$, or $\gamma = 2\cos(\Delta x \xi) - 2$ in terms of trigonometric functions.

In the following, we consider a special case of eq. (B1) with $C_V = C_\sigma = 1$. In this case, we have $\alpha_V = \alpha_\sigma = \frac{\Delta t}{\Delta x}$, denoted with $\alpha$. We also set $\beta_V = \beta_\sigma$ for simplification and denote both terms with $\beta$. Same as in Fig. A1 of Appendix A, we demonstrate the modulus change of $A$ with respect to parameters $\beta$ and $\gamma$ in Fig. B1 for the case $\alpha = 0.5$. For the parameter ranges that we choose, eq. (B3) exhibits one real root and two conjugate complex roots. Fig. B1(a) corresponds to the real root whereas Fig. B1(b) corresponds to the two conjugate complex roots. The interpretation of Fig. B1 is the same as for Fig. A1.

Fig. B1(b) indicates that we should choose $\beta > 0$ in order to provide stabilization, consistent with the intuition that we obtained from the Lax–Wendroff scheme, *cf.* eq. (19). Fig. B1(a) gives us a rough upper bound of parameter $\beta$ at around 0.25. For $\beta > 0.25$, some of the computational modes can be amplified, leading to unstable simulation. We also observe from Fig. B1(a) that computational mode with higher frequency starts to become unstable for smaller $\beta$.

Next, we consider the leapfrog staggered-grid scheme with time filtering on $V$ only, as shown in eq. (B4). The case of filtering $\sigma$ alone is very similar. In fact, for the choice of parameters $C_V = 1$ and $C_\sigma = 1$ in eq. (B1), the two cases are equivalent.

$$\text{(updating)} \qquad \sigma_{i+1/2}^{n+1/2} = \sigma_{i+1/2}^{n-1/2} + \alpha_\sigma (V_{i+1}^n - V_i^n); \tag{B4a}$$

$$\text{(updating)} \qquad \sigma_{i-1/2}^{n+1/2} = \sigma_{i-1/2}^{n-1/2} + \alpha_\sigma (V_i^n - V_{i-1}^n); \tag{B4b}$$

Downloaded from https://academic.oup.com/gji/article/204/3/1443/677722 by guest on 24 April 2024

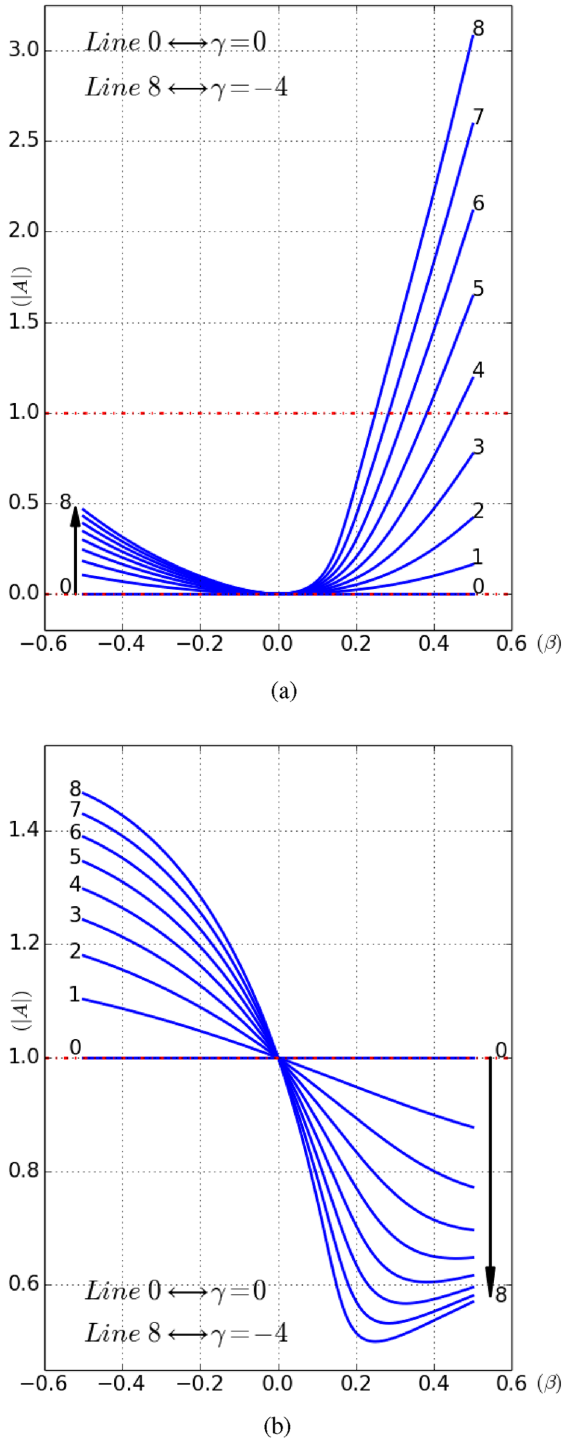


**Figure B1.** Amplitude change of $A$, as roots of eq. (B3), with respect to parameters $\beta$ and $\gamma$. (a) Amplitude of the real root of $A$ (b) Amplitude of the complex roots of $A$

(filtering) $$\overline{V_i^n} = V_i^n + \beta_V \left[ \left( \sigma_{i+1/2}^{n+1/2} - \sigma_{i-1/2}^{n+1/2} \right) - \left( \sigma_{i+1/2}^{n-1/2} - \sigma_{i-1/2}^{n-1/2} \right) \right]; \tag{B4c}$$

(updating) $$V_i^{n+1} = \overline{V_i^n} + \alpha_V \left( \sigma_{i+1/2}^{n+1/2} - \sigma_{i-1/2}^{n+1/2} \right). \tag{B4d}$$

The amplification rate $A$ satisfies the following quadratic equation,

$$A^2 - (2 + \beta_V \alpha_\sigma \gamma + \alpha_V \alpha_\sigma \gamma) A + (1 + \beta_V \alpha_\sigma \gamma) = 0. \tag{B5}$$

Downloaded from https://academic.oup.com/gji/article/204/3/1443/677722 by guest on 24 April 2024

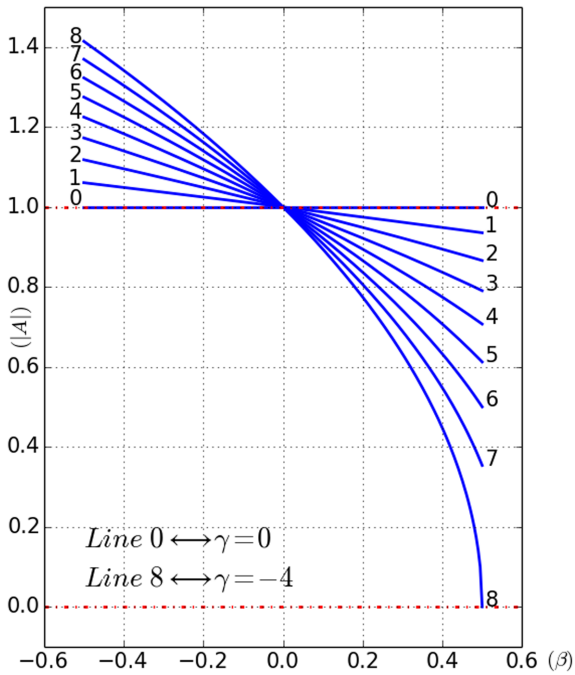


**Figure B2.** Modulus change of $A$, as roots of eq. (B5), with respect to parameters $\beta$ and $\gamma$.

Only two roots exist for eq. (B5), both corresponding to physical modes. Scheme (B4) does not allow computational mode for PDE system (B1). For the parameter ranges that we choose, these two roots are a complex conjugate pair, which have the same modulus. In Fig. B2, we plot the modulus of the two roots against $\beta$ for different values of $\gamma$ for the case $\alpha = 0.5$.

Once again, Fig. B2 indicates that we should choose $\beta > 0$ to provide stabilization. Moreover, scheme (B4) admits bigger range of $\beta$ for stable simulation, compared with scheme (B2). On the other hand, with the same value of $\beta$, scheme (B2) tends to be more effective in damping the high-frequency modes, according to the comparison of Figs B1 and B2. Since the damping effectiveness can be compensated by using bigger $\beta$, we do not observe clear advantage of using scheme (B2), that is, filtering both $V$ and $\sigma$. Therefore, we prefer scheme (B4) over scheme (B2) due to its simplicity and reduced cost.

For scheme (B4), we consider the impact of time filtering on the time step size in the following. The roots $A_1$ and $A_2$ for eq. (B5) can be expressed as follows:

$$A_1 = \frac{2 + \alpha\gamma(\alpha + \beta)}{2} + \frac{\sqrt{\alpha^2\gamma^2(\alpha + \beta)^2 + 4\alpha^2\gamma}}{2}; \tag{B6a}$$

$$A_2 = \frac{2 + \alpha\gamma(\alpha + \beta)}{2} - \frac{\sqrt{\alpha^2\gamma^2(\alpha + \beta)^2 + 4\alpha^2\gamma}}{2}. \tag{B6b}$$

Assuming the discriminant $\alpha^2\gamma^2(\alpha + \beta)^2 + 4\alpha^2\gamma \leq 0$ for all $\gamma \in [-4, 0)$, this leads to relation $\alpha + \beta \leq 1$. In this case, $A_1$ and $A_2$ are a conjugate complex pair, whose amplitude satisfies

$$|A|^2 = 1 + \alpha\beta\gamma. \tag{B7}$$

Since $\gamma < 0$, we conclude that $|A| \leq 1$. Therefore, $\alpha + \beta \leq 1$ is a sufficient condition for stable simulation.

On the other hand, assuming the discriminant $\alpha^2\gamma^2(\alpha + \beta)^2 + 4\alpha^2\gamma > 0$ for some $\gamma \in [-4, 0)$, $A_1$ and $A_2$ will be both real, with $A_1 > A_2$. We need $A_1 \leq 1$ and $A_2 \geq -1$ to have stable simulation. It turns out that $A_1 \leq 1$ is trivially satisfied while $A_2 \geq -1$ leads to requirement $\alpha + \beta \leq \sqrt{\beta^2 - \frac{4}{\gamma}}$ for any $\gamma \in [-4, 0)$. In practice, $\beta$ is usually a small number comparing with $\alpha$ or $-4/\gamma$. Consequently, we omit the $\beta^2$ term in the above inequality relation and arrive at $\alpha + \beta \leq 1$ again.

Therefore, we consider $\alpha + \beta \leq 1$ as the time step restriction of scheme (B4) for system (B1) with parameters $C_V = C_\sigma = 1$ and $\beta_V = \beta_\sigma$. Indeed, application of the time filtering penalizes the time step size. The above analysis can be easily extended to the situation when standard staggered grid scheme is applied to the 2-D or 3-D non-dimensionalized acoustic wave equation in the pressure–velocity formulation with time-filtering similar to eq. (B4c) applied on all velocity components, which leads to the time step restriction $\alpha + \beta \leq \sqrt{1/2}$ and $\alpha + \beta \leq \sqrt{1/3}$, respectively.

Downloaded from https://academic.oup.com/gji/article/204/3/1443/677722 by guest on 24 April 2024